

Solid friction between soft filaments

Andrew Ward¹, Feodor Hilitski¹, Walter Schwenger¹, David Welch², A. W. C. Lau³, Vincenzo Vitelli⁴, L. Mahadevan^{5,6} and Zvonimir Dogic^{1*}

Any macroscopic deformation of a filamentous bundle is necessarily accompanied by local sliding and/or stretching of the constituent filaments^{1,2}. Yet the nature of the sliding friction between two aligned filaments interacting through multiple contacts remains largely unexplored. Here, by directly measuring the sliding forces between two bundled F-actin filaments, we show that these frictional forces are unexpectedly large, scale logarithmically with sliding velocity as in solid-like friction, and exhibit complex dependence on the filaments' overlap length. We also show that a reduction of the frictional force by orders of magnitude, associated with a transition from solid-like friction to Stokes's drag, can be induced by coating F-actin with polymeric brushes. Furthermore, we observe similar transitions in filamentous microtubules and bacterial flagella. Our findings demonstrate how altering a filament's elasticity, structure and interactions can be used to engineer interfilament friction and thus tune the properties of fibrous composite materials.

Filamentous bundles are a ubiquitous structural motif used for the assembly of diverse synthetic, biomimetic and biological materials^{1–4}. Any macroscopic deformation of such bundles is necessarily accompanied by local sliding and/or stretching of the constituent filaments^{4,5}. Consequently, the frictional forces that arise due to interfilament sliding are an essential determinant of the overall mechanical properties of filamentous bundles. Here, we measure frictional forces between filamentous actin (F-actin), which is an essential building block of diverse biological and biomimetic materials. We bundle F-actin filaments by adding the non-adsorbing polymer polyethylene glycol (PEG). As two filaments approach each other, additional free volume becomes available to PEG coils, leading to an effective attraction known as the depletion interaction in physics and chemistry or as macromolecular crowding in biology (Supplementary Fig. 1a; ref. 6). Besides radial interactions, the depletion mechanism also leads to interactions along the filaments' long axes. Although the former have been extensively studied using osmotic stress techniques⁷, little is known about the equally important sliding interactions.

To measure sliding interactions we bundle a pair of actin filaments. Each filament is attached to a gelsolin-coated micrometre-sized bead. Such beads bind exclusively to the barbed end of F-actin, thus determining the attached filament polarity. Two filaments are held together by attractive depletion forces; subsequently, bead 2 is pulled at a constant velocity with an optical trap while the force on bead 1 is simultaneously measured (Fig. 1a,b and Supplementary Movie 1). At first, the force increases as the thermally induced filament slack is pulled out. Subsequently, the force reaches a plateau

and thereafter remains constant even as the interfilament overlap length changes by many micrometres (Fig. 1c). Finally, as the overlap length becomes smaller than a characteristic length scale, the frictional force decreases exponentially and vanishes as the two filaments unbind. Increasing the sliding velocity yields a similar force profile, the only difference being a slightly elevated plateau force F_{\max} . Repeating these experiments at different velocities reveals that F_{\max} exhibits a logarithmic dependence on the sliding velocity (Fig. 1d). The strength and range of the attractive depletion potential is tuned by changing the polymer concentration and size, respectively. This feature allows us to directly relate interfilament sliding friction to cohesive interactions, simply by changing the PEG concentration. Stronger cohesion leads to a larger plateau force, F_{\max} (Fig. 1d).

These experiments reveal several notable features of sliding friction between a pair of F-actin filaments. First, even for the weakest cohesion strength required for assembly of stable bundles, the frictional force is several piconewtons, comparable to the force exerted by myosin motors. Second, above a critical value, the frictional force is independent of the interfilament overlap length. Third, the plateau force, F_{\max} , exhibits a logarithmic dependence on the sliding velocity. These observations are in sharp contrast with models that approximate biopolymers as a structureless filament interacting through excluded-volume interactions. Frictional coupling between such homogeneous filaments would be dominated by hydrodynamic interactions, resulting in forces that are linearly dependent on both the pulling velocity and overlap length, and orders of magnitude weaker than those measured. As these features are not observed experimentally, we exclude hydrodynamic interactions as a dominant source of frictional coupling and reconsider the basic physical processes at work.

Certain aspects of the frictional interactions between actin filaments can be understood by studying the sliding dynamics of two commensurate one-dimensional (1D) lattices of beads and springs under shear (Fig. 2a). The lattices do not slide past each other rigidly. Instead, the mechanism of sliding involves the propagation of localized excitations—called kinks—that carry local compression of the lattice (Fig. 2b). Every time a kink propagates across the filament, the two intercalating lattices slide by one lattice spacing. Sliding happens locally, yielding a frictional force that is controlled by the kink width, λ , rather than the total overlap length, L , provided that $L \gg \lambda$, as is typically the case in conventional friction. However, in our experiments the filament overlap can be controlled from nanometres to many micrometres, allowing us to examine the regime where $L \leq \lambda$. In this regime, a propagating kink cannot fully develop and the sliding force exhibits a dependence on L .

¹Martin Fisher School of Physics, Brandeis University, 415 South Street, Waltham, Massachusetts 02454, USA. ²Graduate Program in Biophysics and Structural Biology, Brandeis University, 415 South Street, Waltham, Massachusetts 02454, USA. ³Department of Physics, Florida Atlantic University, 777 Glades Road, Boca Raton, Florida 33431, USA. ⁴Instituut-Lorentz for Theoretical Physics, Universiteit Leiden, 2300 RA Leiden, The Netherlands. ⁵School of Engineering and Applied Sciences, Harvard University, 29 Oxford Street, Cambridge, Massachusetts 02138, USA. ⁶Department of Physics, Harvard University, 17 Oxford Street, Cambridge, Massachusetts 02138, USA.

*e-mail: zdogic@brandeis.edu

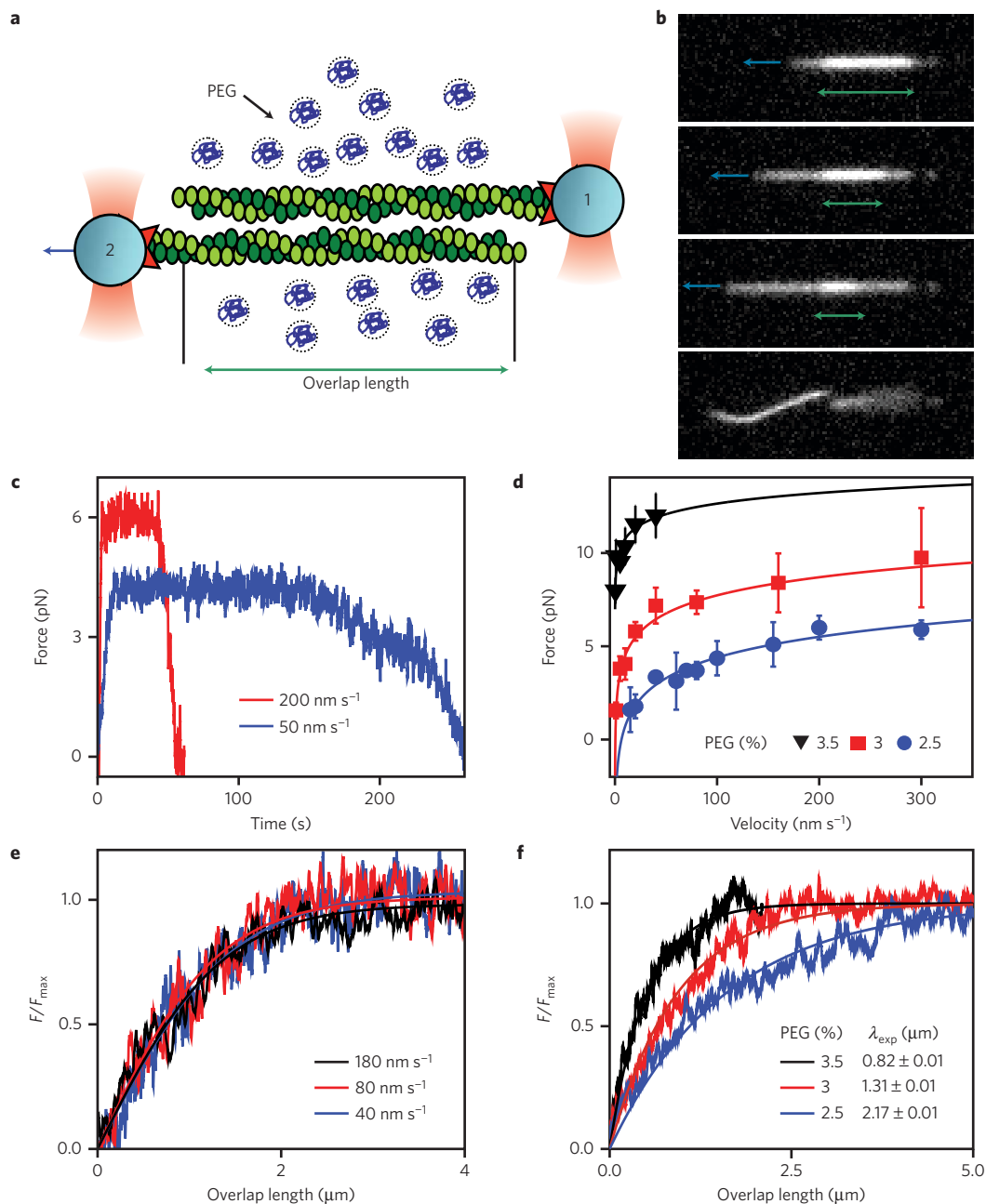


Figure 1 | Single-molecule experiments reveal frictional interactions between a pair of sliding F-actin filaments. **a**, Schematic of the experimental set-up. Actin filaments attached to gelsolin-coated beads are assembled into antiparallel bundles using optical traps. Bead 2 is pulled at a constant velocity while simultaneously measuring the force exerted on bead 1. **b**, Sequence of images illustrating two filaments being pulled apart. The green dashed line indicates the interfilament overlap length and the blue arrow indicates the pulling direction (Supplementary Movie 1). **c**, Time dependence of the frictional force measured for two pulling velocities. **d**, The frictional force, F_{max} , exhibits a logarithmic dependence on the pulling velocity. The measurements are repeated at three different cohesion strengths (PEG concentrations). Error bars indicate the s.e.m., with $n=2-13$ (data points with $n=1$ have no error bars). Lines indicate fits of equation (2) to experimental data. **e**, Dependence of the frictional force F/F_{max} on the interfilament overlap length. Force profiles taken at different sliding velocities rescale onto a universal curve (equation (1)), defining a velocity-independent frictional kink width λ . **f**, As in **e**, but for different PEG concentrations, showing that stronger cohesion leads to a smaller λ . For all experiments, the salt concentration is 200 mM KCl.

These arguments can be quantitatively rationalized within the framework of the Frenkel–Kontorova model^{8,9}. The sliding filament is modelled as a 1D lattice of length L , comprising beads connected by springs with stiffness constant k . The lattice periodicity is given by the actin monomer spacing, d . The interaction with the stationary filament is modelled by a commensurate sinusoidal background potential of depth U_0 and periodicity d . In the continuum limit, the bead displacement field, $u(x)$, satisfies the Sine-Gordon equation, $\lambda^2 u_{xx} = \sin(u(x)/d)$, which admits a static kink solution of the form

$u_s(x) = 4d \tan^{-1}(e^{-x/\lambda})$, where λ is the kink width that corresponds to the length of the lattice that is distorted (see Supplementary Methods). Kink width is determined by the ratio of filament stiffness to the stiffness of the background potential: $\lambda^2 = kd^4/U_0$. For very stiff filaments, such as F-actin, an imposed distortion will extend over many lattice spacings.

We first consider the case $L \leq \lambda$ and assume that the finite size chain located from $x = -L$ to $x = 0$ is gradually pulled out at $x = 0$. The pulling force, F , displaces the rightmost bead to the maximum

of the potential (that is, $u(0) = d/2$) generating a strain field, $u_x(x)$, that decays exponentially inside the sample with a characteristic length λ . Once the rightmost bead hops over the maximum in the potential, the whole lattice slides by d and every bead falls to the bottom of the respective potential, generating a state of vanishing strain and energy. Repeating this process n times translates the leftmost edge from $-L$ to $-L + nd$. The work done by the pulling force in the n th run, $F(n)d$, is the energy difference between the elastic energy stored in the kink configuration $u_s(x)$ and the uniform state $u(x) = 0$, which has zero energy. Because the elastic energy is proportional to $F_{\max}d \operatorname{sech}^2(x/\lambda)$ over the part of the chain still interacting with the background potential (that is, from $x = L + nd$ to $x = 0$), the resulting force reads:

$$F(n) = F_{\max} \tanh\left(\frac{L - nd}{\lambda}\right) \quad (1)$$

where $L - nd$ represents the remaining overlap length between the two filaments. If the overlap length is larger than the kink width ($L > \lambda$), $F(n)$ saturates at F_{\max} . In this limit, a kink nucleated at the rightmost edge can fully develop and propagate down the chain, progressively shifting the particles it leaves behind (see Supplementary Fig. 2 and Supplementary Movie 2). As a result the force ceases to depend on the overlap length. Instead, it is set by the kink width, which remains equal to the static value λ , unaffected by the kink dynamics in the overdamped regime (see Supplementary Information).

Experiments reveal that F_{\max} scales logarithmically with the pulling speed, v (Fig. 1d). The intuitive reason for this dependence is that, as the lattice is pulled, the particles within the kink undergo thermally assisted hopping through the periodic background potential. A classical model, originally formulated by Prandtl and Tomlinson, predicts:

$$F_{\max} = \frac{k_B T}{d} \log\left(\frac{v}{2df_c} e^{U_0/k_B T}\right) \quad (2)$$

where T is the temperature and $1/f_c$ is the relaxation time of a monomer in a potential energy well^{10–13}. Fitting equation (2) to the plateau value of the force–velocity curves reveals that the periodicity of the background potential is ~ 5 nm (Supplementary Table 1), in quantitative agreement with the F-actin monomer spacing¹⁴. This result suggests that cohering F-actin monomers intercalate with each other, and that sliding interactions require monomers to either deform or hop over each other.

Equation (1) predicts that the force profiles taken at varying pulling speeds should fall onto a master curve once rescaled by $F_{\max}(v)$. This data collapse is demonstrated in Fig. 1e (Supplementary Table 2). It yields an experimental measurement of velocity-independent kink width, λ , which we compare to the theoretical prediction $\lambda = \sqrt{kd^4/U_0}$. We take the lattice periodicity to be 5.5 nm (ref. 14) and k to be $\sim 7,000$ pN nm^{−1} (ref. 15). To estimate U_0 we measure the strength of the depletion-induced attraction by allowing an isolated filament to fold into a racquet-like configuration (Supplementary Fig. 1c,d; ref. 16). The size of the racquet head is directly related to the filament cohesion strength per unit length, U_0 . Without any adjustable parameters our theoretical model predicts values of λ which are of the same order of magnitude as those extracted from experiments (Supplementary Table 3). Increasing depletant concentration increases U_0 , leading to a decrease in λ , which is again in agreement with the theoretical prediction. In summary, we have demonstrated that the tunable kink width critically determines the dependence of frictional force on the overlap length between the two intercalating nanofilaments. A length scale similar to λ arises in many other materials science contexts, such as shearing of double stranded DNA (refs 17,18).

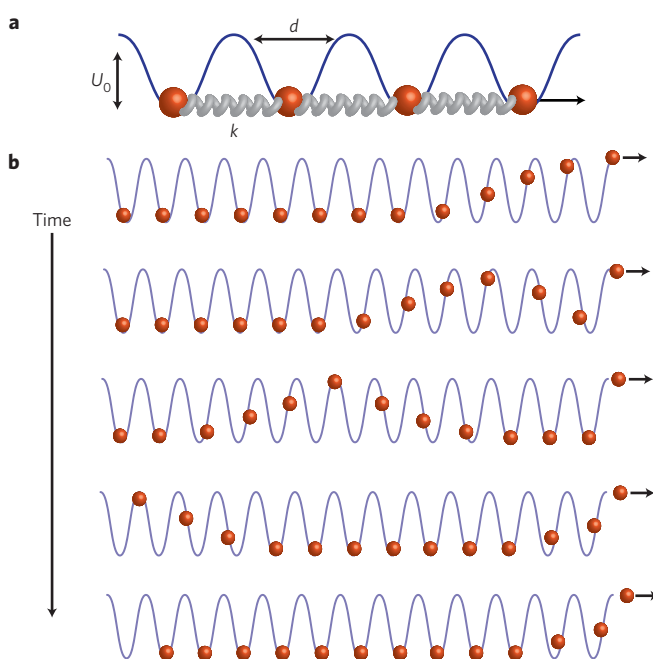


Figure 2 | 1D-Frenkel-Kontorova model accounts for the essential features of interfilament sliding friction. a, Schematic of a model in which a sliding filament is approximated as a periodic lattice of points connected by stiff springs. A sinusoidal background potential models the interaction with the stationary filament. **b**, Schematic of how a filament slides by one lattice spacing in a response to an applied pulling force (Supplementary Movie 2). For filaments with finite extensibility the applied force decays over a characteristic length scale that is determined by the ratio of spring stiffness to the stiffness of the background potential. The first bead hopping over the rightmost barrier is accompanied by soliton formation that propagates leftwards. Once the soliton reaches the leftmost bead, the entire filament is translated by a lattice spacing d .

Previous experiments have uncovered directionally dependent friction in both biological and synthetic materials^{19–21}. To investigate the directional dependence of interfilament sliding friction between polar actin filaments we have altered the experimental configuration by attaching beads to both ends of one filament (Supplementary Fig. 3). Using this configuration we find that F_{\max} for sliding antiparallel filaments is approximately twice as large as in filaments with parallel alignment (Fig. 3a,b). Whereas F_{\max} is different, the scaling of frictional force with velocity and filament overlap length is the same for both orientations, indicating that same physics describes sliding of both polar and anti-polar filaments. Furthermore, we also investigate stress relaxation on application of a step strain (Fig. 3c). For parallel orientation the applied stress quickly relaxes to a finite but small force. In contrast, for antiparallel orientation the applied stress relaxes on much longer timescales. These experiments indicate that the axial interaction potential between sliding F-actin filaments is polar; thus, sliding actin filaments can act as molecular ratchets (Fig. 3d).

Armed with a basic understanding of filament sliding friction, we next devise practical methods to tune its magnitude. One possible method to accomplish this is by changing the filament structure. We decorated F-actin with a covalently attached PEG brush. In this system, friction was quantified by visualizing sliding dynamics of bundled filaments. Native F-actin bundles exhibited no thermally driven sliding, in agreement with our previous measurements (Fig. 4a). In contrast, PEG-coated F-actin formed bundles in which individual filaments freely slid past each other owing to thermal fluctuations (Fig. 4b and Supplementary Movie 3). To extract

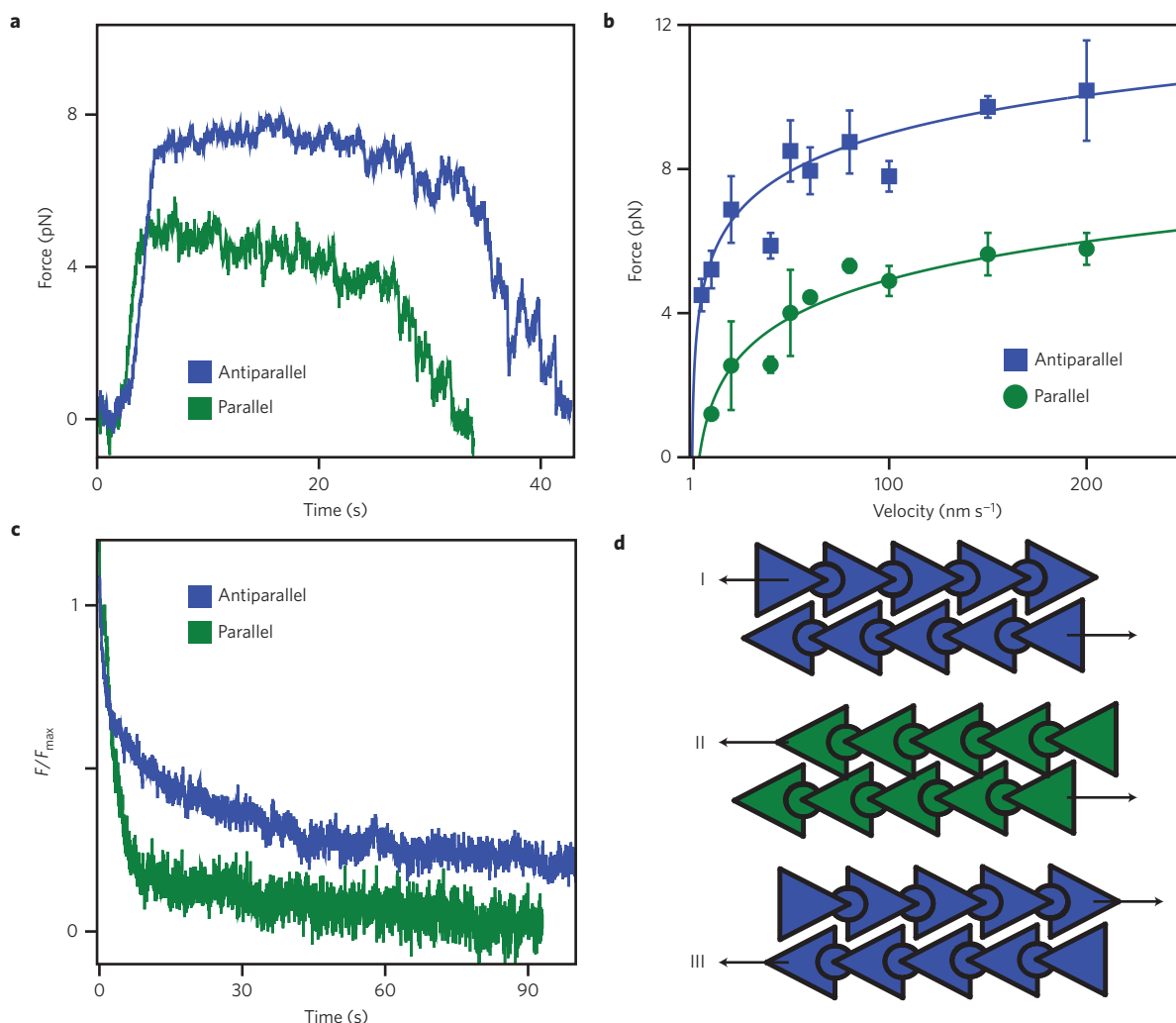


Figure 3 | Interfilament sliding friction depends on relative filament polarity. **a**, Two profiles describing the time-dependent frictional force. The only difference is the relative filament polarity. **b**, The plateau force, F_{\max} , exhibits a pronounced directional dependence. Error bars indicate the s.e.m., with $n=2-13$ (data points with $n=1$ have no error bars). **c**, Relaxation of the force on application of a step strain. For parallel filaments the force quickly relaxes to a small but finite value. For antiparallel filaments the force relaxes on much longer timescales. **d**, Schematic representation of actin filaments that account for the directional dependence of sliding friction. Antiparallel and parallel arrangements correspond to schemes I and II, respectively. We are not able to measure friction for configuration III. All experiments were performed at a salt concentration of 400 mM KCl.

quantitative data, we measure the mean square displacement (MSD) of the relative position of the short filament with respect to the longer filament to which it is bound (Fig. 4c). The linear MSD curves are consistent with hydrodynamic coupling between PEG-coated filaments; the slope yields the diffusion of a bound filament, which is a factor of five smaller than that of an isolated filament²². It follows that the hydrodynamic friction coefficient of a bundled 5 μm -long filament is $\sim 10^{-4}$ pN s nm⁻¹. Pulling such a filament at 100 nm s⁻¹ would result in a 10 fN force, which is three orders of magnitude smaller than the comparable forces measured for bare F-actin. This demonstrates how simple structural modifications greatly alter the sliding filament friction. We compare these results with those for another important biopolymer, a microtubule. Previous work has shown that, unlike F-actin, the sliding friction of a microtubule is weak and dominated by hydrodynamic interactions (Fig. 4d; ref. 23). Microtubule surfaces are coated with charged disordered amino-acid domains, known as e-hooks²⁴. We hypothesized that these domains might act as an effective polyelectrolyte brush, screening molecular interactions and thus lowering sliding friction. To test this hypothesis we remove e-hooks with an appropriate protease. When treated in such a way, microtubule bundles exhibit no interfilament

sliding, indicating a much higher sliding friction (Fig. 4e,f). Such observations agree with previous studies that have shown that brush-like surfaces can drastically lower friction coefficients²⁵.

Alternatively, frictional coupling can be tuned by engineering lateral interfilament interactions. We examined how the sliding dynamics of three different filaments (F-actin, microtubules, bacterial flagella) depend on the strength of lateral filament attraction, which is controlled by the depletant concentration, and on the average filament separation, which is tuned by the ionic strength (Fig. 5). Microtubules and bacterial flagella exhibited two distinct dynamical states. For low depletant concentration (weak attraction) and low ionic strength the filaments have large lateral separations and freely slide past each other. Such dynamics indicates weak frictional coupling that is dominated by hydrodynamic interactions. Increasing depletant concentration or ionic strength above a critical threshold induces a sharp transition into a distinct dynamical state that exhibits no measurable sliding even after tens of minutes of observation time. The sliding dynamics of flagella and microtubules are remarkably similar to each other. In comparison, native F-actin filaments showed only a non-sliding state indicative of solid-like friction, for all parameters explored. The observation

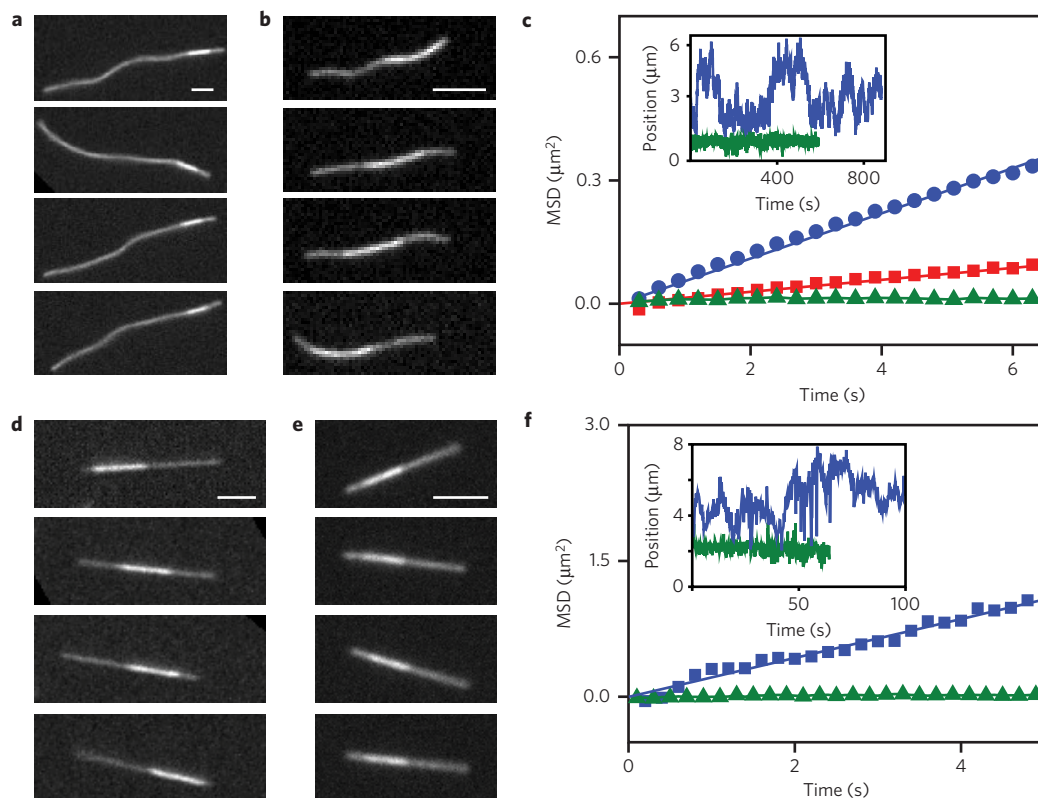


Figure 4 | Filament surface structure controls the transition from solid to hydrodynamic friction. **a**, Sequence of images illustrating the relative diffusion of a bundled pair of unmodified F-actin filaments. The brighter region, indicating the filament overlap area, is frozen at a specific location owing to the absence of any thermally induced filament sliding. **b**, F-actin filaments coated with a PEG polymer brush exhibit thermally driven sliding, owing to a significantly reduced frictional coupling (Supplementary Movie 3). **c**, For PEG-coated bundles of different lengths the mean square displacement (MSD) of the short filament with respect to the longer filament increases linearly with time, indicating a hydrodynamic coupling. Shown are MSDs of a 6- μm -long filament (red squares) and 3.7 μm -long filament (blue circles). Uncoated filaments (green triangles) exhibit a flat MSD. Inset: Relative position of a filament diffusing within the bundle for both coated (blue) and uncoated (green) F-actin. **d**, Untreated microtubule bundles exhibit diffusive sliding that is dominated by hydrodynamic coupling. **e**, Removing brush-like e-hooks from the microtubule surface leads to bundles that exhibit no sliding. **f**, MSDs of a bundle of microtubules (blue) compared with a bundle of subtilisin-treated microtubules (green). Inset: Relative position of a microtubule bundle for both untreated (blue) and subtilisin-treated microtubule (green). Scale bars, 3 μm .

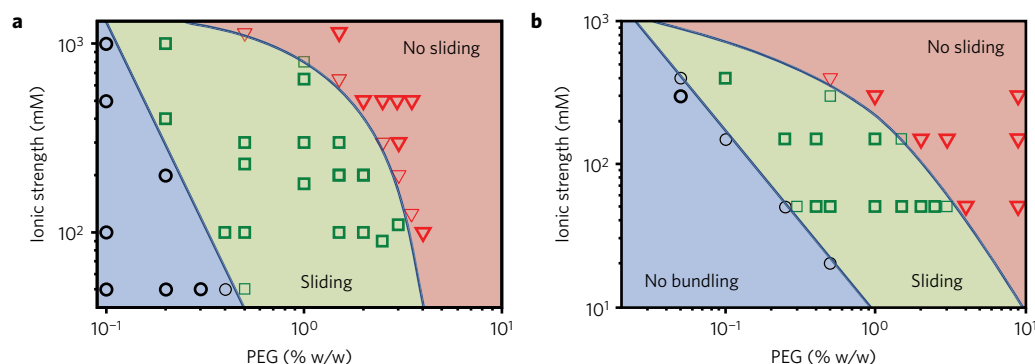


Figure 5 | Sliding dynamics of microtubules and bacterial flagella. **a**, Microtubule sliding dynamics depends on the depletant concentration and the suspension's ionic strength. At low depletant concentration and ionic strength, filaments remain unbundled (blue circles). To induce bundle formation it is necessary to either increase the depletant concentration or decrease the electrostatic screening length. In this regime, bundles exhibit sliding dynamics (green squares). With increasing ionic strength or depletant concentration, sliding filaments undergo a sharp crossover into a state with no detectable sliding, indicating a stronger frictional coupling (red triangles). **b**, Straight bundled flagellar filaments exhibit sliding similar to that of microtubule bundles.

of non-sliding dynamics in three structurally diverse filaments suggests that solid-like frictional coupling is a common feature of biological filaments.

To summarize, the mechanical properties of composite filamentous bundles are determined not only by the rigidity of the constituent filaments but also by their interfilament interactions, such as

the cohesion strength and sliding friction²⁶. Therefore, quantitative models of composite bundle mechanics must account for inter-filament sliding friction. We have demonstrated an experimental technique that enables the measurement of such forces. We directly measured frictional forces between chemically identical F-actin filaments, thus bridging the gap between the previously studied

friction of sliding point-like contacts^{27,28} and 2D surfaces^{29–31}. Combining such measurements with simulations and theoretical modelling, we have described the design principles required to engineer interfilament friction and thus tune the properties of frictionally interacting composite filamentous materials.

Methods

Actin and gelsolin were purified according to previously published protocols. Actin filaments were polymerized in high-salt buffer and subsequently stabilized with Alexa-488-phalloidin. Gelsolin was covalently coupled to 1 µm carboxylic-coated silica beads by 1-ethyl-3-[3-dimethylaminopropyl]carbodiimide hydrochloride. All experiments were performed in a buffer suspension containing 20 mM phosphate at pH = 7.5, 300 mg ml⁻¹ sucrose and either 200 mM or 400 mM KCl. Poly (ethylene glycol) (MW 20,000 Da) was used as a depletion agent at concentrations ranging between 20 and 35 mg ml⁻¹, as indicated in the main text. An optical trap (1,064 nm) was time-shared between multiple positions using an acousto-optic Deflector. One bead was translated at a constant velocity while the force exerted on the other bead was measured using a back-focal-plane interferometry technique. Simultaneously, images of sliding F-actin filaments were acquired using fluorescence microscopy on a Nikon Eclipse Te2000-u microscope equipped with an Andor iKon-M charge-coupled detector. Sliding dynamics was visualized by confining a two-filament bundle in a quasi-2D microscope chamber, thus ensuring that filaments stay in focus. The surfaces were coated with a polyacrylamide brush, which suppresses adsorption of filaments. Bacterial flagella were isolated from *Salmonella typhimurium* strain SJW 605. The flagellin protein of these bacteria has a mutation that causes flagellar filaments to assume a straight shape. Microtubules were isolated following standard protocols.

Received 28 February 2013; accepted 20 January 2015;
published online 2 March 2015

References

- Vigolo, B. *et al.* Macroscopic fibres and ribbons of oriented carbon nanotubes. *Science* **290**, 1331–1334 (2000).
- Sanchez, T., Chen, D. T. N., DeCamp, S. J., Heymann, M. & Dogic, Z. Spontaneous motion in hierarchically assembled active matter. *Nature* **491**, 431–434 (2012).
- Kozlov, A. S., Baumgart, J., Risler, T., Versteegh, C. P. C. & Hudspeth, A. J. Forces between clustered stereocilia minimize friction in the ear on a subnanometre scale. *Nature* **474**, 376–379 (2011).
- Claessens, M., Bathe, M., Frey, E. & Bausch, A. R. Actin-binding proteins sensitively mediate F-actin bundle stiffness. *Nature Mater.* **5**, 748–753 (2006).
- Heussinger, C., Bathe, M. & Frey, E. Statistical mechanics of semiflexible bundles of wormlike polymer chains. *Phys. Rev. Lett.* **99**, 048101 (2007).
- Zimmerman, S. B. & Minton, A. P. Macromolecular crowding—biochemical, biophysical and physiological consequences. *Annu. Rev. Biophys. Biomol. Struct.* **22**, 27–65 (1993).
- Rau, D. C., Lee, B. & Parsegian, V. A. Measurement of the repulsive force between poly-electrolyte molecules in ionic solution—hydration forces between parallel DNA double helices. *Proc. Natl Acad. Sci. USA* **81**, 2621–2625 (1984).
- Vanossi, A., Manini, N., Urbakh, M., Zapperi, S. & Tosatti, E. Colloquium: Modeling friction: From nanoscale to mesoscale. *Rev. Mod. Phys.* **85**, 529–552 (2013).
- Braun, O. M. & Kivshar, Y. S. Nonlinear dynamics of the Frenkel–Kontorova model. *Phys. Rep.* **306**, 1–108 (1998).
- Merkel, R., Nassoy, P., Leung, A., Ritchie, K. & Evans, E. Energy landscapes of receptor–ligand bonds explored with dynamic force spectroscopy. *Nature* **397**, 50–53 (1999).
- Gnecco, E. *et al.* Velocity dependence of atomic friction. *Phys. Rev. Lett.* **84**, 1172–1175 (2000).
- Muser, M. H., Urbakh, M. & Robbins, M. O. in *Advances in Chemical Physics* Vol. 126 (eds Prigogine, I. & Rice, S. A.) 187–272 (John Wiley, 2003).
- Suda, H. Origin of friction derived from rupture dynamics. *Langmuir* **17**, 6045–6047 (2001).
- Holmes, K. C., Popp, D., Gebhard, W. & Kabsch, W. Atomic model of the actin filament. *Nature* **347**, 44–49 (1990).
- Kojima, H., Ishijima, A. & Yanagida, T. Direct measurement of stiffness of single actin-filaments with and without topomyosin by *in-vitro* nanomanipulation. *Proc. Natl Acad. Sci. USA* **91**, 12962–12966 (1994).
- Lau, A. W. C., Prasad, A. & Dogic, Z. Condensation of isolated semi-flexible filaments driven by depletion interactions. *Europhys. Lett.* **87**, 48006 (2009).
- De Gennes, P. G. Maximum pull out force on DNA hybrids. *C. R. Acad. Sci. IV* **2**, 1505–1508 (2001).
- Hatch, K., Danilowicz, C., Coljee, V. & Prentiss, M. Demonstration that the shear force required to separate short double-stranded DNA does not increase significantly with sequence length for sequences longer than 25 base pairs. *Phys. Rev. E* **78**, 011920 (2008).
- Bormuth, V., Varga, V., Howard, J. & Schaffer, E. Protein friction limits diffusive and directed movements of kinesin motors on microtubules. *Science* **325**, 870–873 (2009).
- Choi, J. S. *et al.* Friction anisotropy-driven domain imaging on exfoliated monolayer graphene. *Science* **333**, 607–610 (2011).
- Forth, S., Hsia, K.-C., Shimamoto, Y. & Kapoor, T. M. Asymmetric friction of nonmotor MAPs can lead to their directional motion in active microtubule networks. *Cell* **157**, 420–432 (2014).
- Li, G. L. & Tang, J. X. Diffusion of actin filaments within a thin layer between two walls. *Phys. Rev. E* **69**, 061921 (2004).
- Sanchez, T., Welch, D., Nicastro, D. & Dogic, Z. Cilia-like beating of active microtubule bundles. *Science* **333**, 456–459 (2011).
- Nogales, E., Wolf, S. G. & Downing, K. H. Structure of the $\alpha\beta$ tubulin dimer by electron crystallography. *Nature* **391**, 199–203 (1998).
- Klein, J., Kumacheva, E., Mahalu, D., Perahia, D. & Fetters, L. J. Reduction of frictional forces between solid-surfaces bearing polymer brushes. *Nature* **370**, 634–636 (1994).
- Akbulut, M., Belman, N., Golan, Y. & Israelachvili, J. Frictional properties of confined nanorods. *Adv. Mater.* **18**, 2589–2592 (2006).
- Mate, C. M., McClelland, G. M., Erlandsson, R. & Chiang, S. Atomic scale-friction of a tungsten tip on a graphite surface. *Phys. Rev. Lett.* **59**, 1942–1945 (1987).
- Luan, B. Q. & Robbins, M. O. The breakdown of continuum models for mechanical contacts. *Nature* **435**, 929–932 (2005).
- Yoshizawa, H., Chen, Y. L. & Israelachvili, J. Fundamental mechanism of interfacial friction. 1. Relation between adhesion and friction. *J. Phys. Chem.* **97**, 4128–4140 (1993).
- Van Alsten, J. & Granick, S. Molecular tribometry of ultrathin liquid-films. *Phys. Rev. Lett.* **61**, 2570–2573 (1988).
- Bohlein, T., Mikhael, J. & Bechinger, C. Observation of kinks and antikinks in colloidal monolayers driven across ordered surfaces. *Nature Mater.* **11**, 126–130 (2012).

Acknowledgements

We acknowledge useful discussions with N. Upadhyaya, M. Hagan and R. Bruinsma. A.W., D.W. and W.S. were supported by National Science Foundation grants CMMI-1068566, NSF-MRI-0923057 and NSF-MRSEC-1206146. F.H. and Z.D. were supported by Department of Energy, Office of Basic Energy Sciences under Award DE-SC0010432TDD. V.V. acknowledges FOM and NWO for financial support. L.M. was supported by Harvard-NSF MRSEC and the MacArthur Foundation. We also acknowledge use of the Brandeis MRSEC optical microscopy facility (NSF-MRSEC-1206146).

Author contributions

A.W. and Z.D. conceived the experiments. A.W. measured actin sliding friction and performed computer simulations. F.H., A.W. and D.W. performed microtubule sliding experiments. W.S. performed flagella sliding dynamics. A.W.C.L. developed a preliminary theoretical model that explains the velocity dependence of sliding friction. L.M. and V.V. developed the theoretical model that explains the dependence of sliding friction on overlap length. A.W., V.V., L.M. and Z.D. wrote the manuscript. All authors revised the manuscript.

Additional information

Supplementary information is available in the [online version of the paper](http://www.nature.com/paper). Reprints and permissions information is available online at www.nature.com/reprints. Correspondence and requests for materials should be addressed to Z.D.

Competing financial interests

The authors declare no competing financial interests.

Solid friction between soft filaments

Supplementary Methods:

Actin purification and handling: Monomeric G-actin was isolated from frozen chicken skeletal muscle (Pel-Freeze) following the standard protocol^{1,2}. To eliminate any oligomers, G-actin was subsequently purified on a size exclusion column (Sephacryl S-200HR, GE Healthcare) and stored in G buffer (2 mM HEPES, 0.2 mM ATP, 0.2 mM CaCl₂, pH 7.5) at -80°. Filamentous F-actin was polymerized by dissolving G-actin monomers in F-Buffer (10 mM HEPES, 150 mM KCl, 2 mM MgCl₂, 1 mM DTT, pH 7.5). F-actin was labeled with Alexa-488-phalloidin (Molecular Probes) at an equi-molar dye to monomer ratio³. All samples were prepared in buffer containing 30% sucrose w/w, 20 mM phosphate pH 7.5 and either 200 or 400 mM KCl as indicated in the text. Sucrose slows the desorption rate of Alexa-488-phalloidin thus prolonging sample lifetimes⁴. To suppress photobleaching an oxygen scavenging system was used at final concentration of 5 mM DTT, 3 mg/ml glucose, 20 µg/ml glucose oxidase, and 3.5 µg/ml catalase. Gelsolin was purified from rabbit plasma (Pel-Freeze) according to previously published protocol⁵.

Gelsolin coated beads: The actin filaments were attached to a silica bead using gelsolin, a protein that strongly binds to the filament's barbed end⁶. Gelsolin was covalently attached to silica beads using a modification of previously published protocol⁶. Carboxylated beads (10 mg of 1 µm diameter, Bangs Beads) were suspended in 1 mL of deionized water. The beads were centrifuged twice (1500 g for 5 minutes) and re-suspended in deionized water. Subsequently, they were washed three more times and each time were resuspended in 1 mL of 2-(N-morpholino) ethanesulfonic acid (MES) buffer (50 mM, pH 6.0). After the final spin, the beads were resuspended in 1 mL of MES buffer containing 0.4 mg 1-Ethyl-3-(3-dimethylaminopropyl) carbodiimide (EDC) and 0.6 mg N-hydroxysuccinimide (NHS). They were gently mixed on a slow rotator for 15 min, spun down twice to remove excess reagent, and resuspended in 0.5 mL of phosphate buffer (20 mM, pH 7.4). The coated beads were sonicated with a tip sonicator to reduce bead aggregation. At this time gelsolin (10-40 µg in phosphate buffer (0.5mL, 20 mM, pH 7.4)) was added to the beads. The resulting mixture was slowly stirred for 5 to 8 hours at 4°. The gelsolin coated beads were spun down twice to remove any

unbound gelsolin and were re-suspended in phosphate buffer (20 mM, pH 7.4, 10 mg/ml BSA). When stored at 4°, gelsolin labeled beads remained active for up to 3 months.

Since calcium affects gelsolin activity, the experiments were performed in presence of 1 μ M CaCl_2 . A trapped gelsolin coated bead was brought into the vicinity of an actin filament. Gelsolin initially attaches to the filament sideways. In a subsequent slower step it severs the filament resulting in an end-capped filament-bead construct. The time lag between sideways attachment and severing can be up to a few minutes. For filaments under tension the severing time is usually faster. Since gelsolin only binds the barbed end, the polarity of the attached filament is immediately known.

Microtubule preparation: Alexa-647 labeled tubulin was mixed with unlabeled tubulin at a 1:9 ratio to a final concentration of 1 mg/mL in buffer containing 80 mM PIPES pH 6.8, 1 mM EGTA, 2 mM MgCl_2) Polymerization was initiated by the addition of GMPCPP to a final concentration of 0.5 mM, and subsequently incubating at 37 °C for 2 hours. This mixture was aliquoted and frozen at -80 °C for future use. Aliquots were diluted at a ratio of 3:20 and incubated at 37 °C for 2 hours. To cleave the C-terminus tails of tubulin subtilisin (P8038 Sigma) was added to a concentration of 1.5 mg/mL and incubated at 30 °C for 1 hour. Subtilisin activity was stopped by the addition of Phenylmethanesulfonyl fluoride to a final concentration of 1mM. Subsequently, the solution was then spun through a 60% glycerol solution cushion for 20 minutes at 80k rpm, and then resuspended to 0.15 mg/mL.

Instrumentation: Filament sliding experiments were performed using a time-shared optical trap. A trapping laser beam (1064 nm, Coherent Compass) was brought into the optical path of an inverted microscope (Nikon Eclipse Te2000-u) and focused with a 100X objective onto the image plane (Nikon PlanFlour, NA 1.3). To simultaneously trap multiple beads, a single beam was shared between different positions using an acousto-optic deflector (IntraAction-276HD)⁷. Bead position was determined with back focal plane interferometry using an 830 nm laser as a detection beam (Point Source, IFlex-2000)⁸. Trap stiffness was calibrated by analyzing the power spectrum of the bead position⁸. We detected position in two orthogonal directions corresponding to the directions in which we manipulate the traps. In all sliding experiments we pulled in the same direction using only 1 axis of the AOD, ensuring that force is along this direction. The lack of alignment between the QPD and the axis of the AOD makes

underestimate of the frictional force possible. However, computing the net force using both X and Y directions changed the force by less than 1%. Custom Labview software acquired images of sliding fluorescently labeled F-actin filaments while simultaneously recording the bead positions through a DAQ board (National Instruments PCI-6251). Cooled CCD device was used for image acquisition (Andor iKon-M).

Controlling polarity of filament bundle: A gelsolin coated bead can only be attached to the barbed end of a filament. In order to investigate the influence of filament polarity on sliding friction, we developed a strategy for attaching beads to both ends of the same filament. To create such a construct we first assemble two regular F-actin-bead constructs in which filaments are attached at their barbed ends. Subsequently, we bundle them together via the depletion forces (Fig. S3). To ensure that there is no slippage in this connection we add up to 7 short filaments to the bundle. The stability of such a construct was tested by placing it under a tension of 10 pN. The actin linkage could sustain this load without any detectable slippage. Controlling both ends of one filament allowed us to determine dependence of sliding friction on relative filament polarity.

Decorating F-actin filament with a PEG brush: F-actin filaments were coated with a PEG brush (mPEG-SPA, MW 2000, Nektar) which covalently binds to primary amines located on the filament surface by the N-Hydroxysuccinimide group. F-actin was polymerized and fluorescently labeled as described previously. Subsequently, filaments were mixed with a solution of mPEG-SPA in F-Buffer (pH=7.5) at a 10:1 PEG:actin monomer ratio. The solution was allowed to incubate at 4° C for 3 hours.

Simulations of filament sliding: Sliding F-actin filament is modeled by a series of beads connected with springs. The filament is moving along a background sinusoidal potential, which is commensurate with the filament periodicity (Fig. S3A). Outside the region of the initial filament overlap the background potential is flat. The behavior of such a model is examined with overdamped molecular dynamics simulations⁹. We use dimensionless units in which forces are rescaled by $k_B T/d$, potential energy by $k_B T$, and time by $d^3 \eta/k_B T$. The stiffness of the springs connecting the beads varies between 100-600 ($k_B T/d^2$), and the bead size is $0.6d$. The height of the potential varies between 2-15 $k_B T$. Simulations illustrate the mechanism by which the filament translocation takes place. Pulling the rightmost bead over the final barrier is

accompanied by the soliton formation which carries local lattice compression leftwards along the filament contour length (Supplementary Movie S2). Once the soliton reaches the leftmost bead the entire filaments translocated by a one-lattice spacing.

Theoretical model of kink structure and dynamics: We outline intermediate steps that lead to Eq. (1) of main text. We exploit a perturbative approach that illustrates how, once formed, the kink can move retaining its static profile (see Ref. 10). We consider the driven stochastic sine-Gordon equation in the overdamped limit, appropriate for the experimental regime:

$$-\phi'' + \frac{1}{\lambda^2} \sin(\phi) = -\alpha \dot{\phi} - F + \eta(x, t), \quad (1)$$

where $\phi(x, t)$ is the displacement field, α is the drag coefficient, F is a constant applied force and $\eta(x, t)$ is a random fluctuating force modeling thermal noise. None of the terms on the right hand side were explicitly considered in the main text. If the pulling and random forces are small perturbations we can assume that the soliton retains its static shape and the effect of the force results in a translation over time of the position of the center of the soliton, denoted by the collective coordinate $X(t)$. To leading order in perturbation theory, we obtain a solution of the form:

$$\phi(x, t) = 4 \tan^2 \left(e^{\frac{x-X(t)}{\lambda}} \right) \quad (2)$$

Note that if inertia effects were present a Lorentz contraction of the kink width would be possible in the limit in which the kink moves close to the sound speed. However, these effects are not relevant in the overdamped limit. The total energy stored in the field can be obtained by substituting Eq. (2) into the following expression:

$$E = \int dx \left(\frac{1}{2} (\phi')^2 + \frac{1}{\lambda^2} (1 - \cos \phi) \right) \quad (3)$$

If we assume for simplicity that $X(t)=0$ and denote the limits of integration by L_2 and L_1 , we obtain:

$$E = \frac{4}{\lambda^2} \int_{L_1}^{L_2} dx \operatorname{sech}^2(x) = \frac{4}{\lambda^2} \tanh(L_2 - L_1) \quad (4)$$

This relation predicts how the sliding force will scale with filament overlap length.

Next we exploit a perturbative approach that illustrates how, once formed, the kink can move while retaining its static profile. When the overlap length is much smaller than the kink width, sliding takes place by a motion of the kink that we now model according to the overdamped dynamics of Eq. 1. First, we multiply both side of Eq. 1 with $\dot{\phi}$ and integrate with respect to x to obtain:

$$\int dx(-\dot{\phi}\phi'' + \frac{1}{\lambda^2}\dot{\phi}\sin(\phi)) = \int dx(-\alpha(\dot{\phi})^2 - F\dot{\phi} + \eta(x,t)\dot{\phi}) \quad (5)$$

Next we take a time derivative of Eq. 3, integrate by parts the first term and use the left hand side of Eq. 5 to obtain

$$\frac{dE}{dt} = \int dx(-\alpha(\dot{\phi})^2 - F\dot{\phi} + \eta(x,t)\dot{\phi}) \quad (6)$$

If the kink width is much smaller than the domain of integration and the center of kink is far from the boundary, E is approximately constant over time, making the left hand side of Eq. 6 equal to zero. Next, we substitute the ansatz (Eq. 2) for the kink profile $\phi(x,t)$ into Eq. 6 and obtain a Langevin equation for $X(t)$ where the statistics of the noise term must be suitably modified [1]:

$$\alpha\dot{X} - \frac{\pi}{4m}F + \frac{\pi}{4m}\xi = 0. \quad (7)$$

We can further add the gradient of the Peierl-Nabarro potential barrier $V_{PN}(X)$ on the right hand side of the above equation:

$$V_{PN}(X) = \frac{1}{2}E_{PN}(1 - \cos(x)). \quad (8)$$

Note however that E_{PN} is exponentially suppressed in the experimentally relevant limit for which the kink width is large compared to lattice spacing¹⁰. Hence, within the simplified model considered here the kink can be viewed as particle whose spatial profile is described by the static solution in Eq. (2) translating at a speed \dot{X} . If the noise ξ in Eq. 7 is ignored or averages to zero, we obtain a constant average speed $\dot{X} \approx \frac{\pi}{4m\alpha}F$ (see Supplementary movie S2).

Supplementary Figures

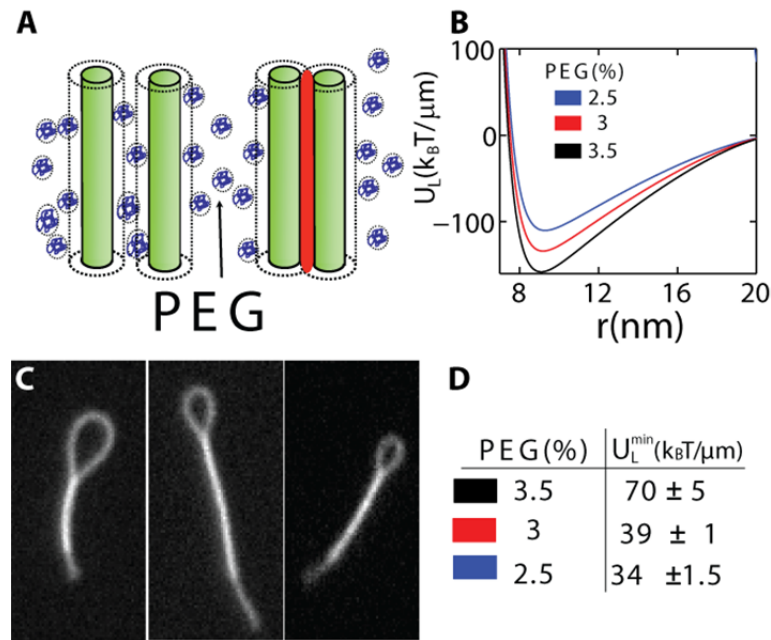
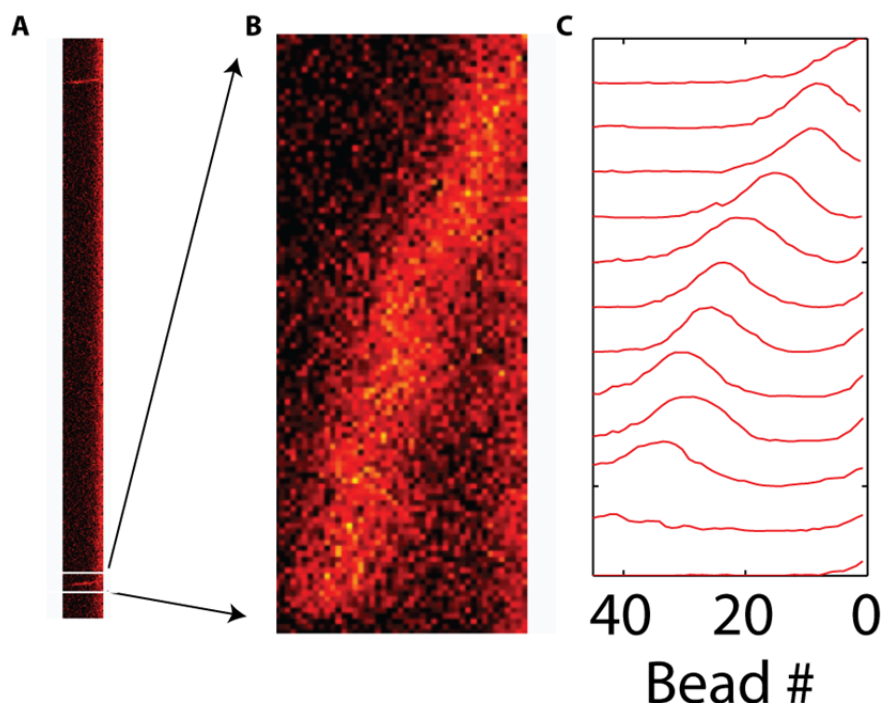
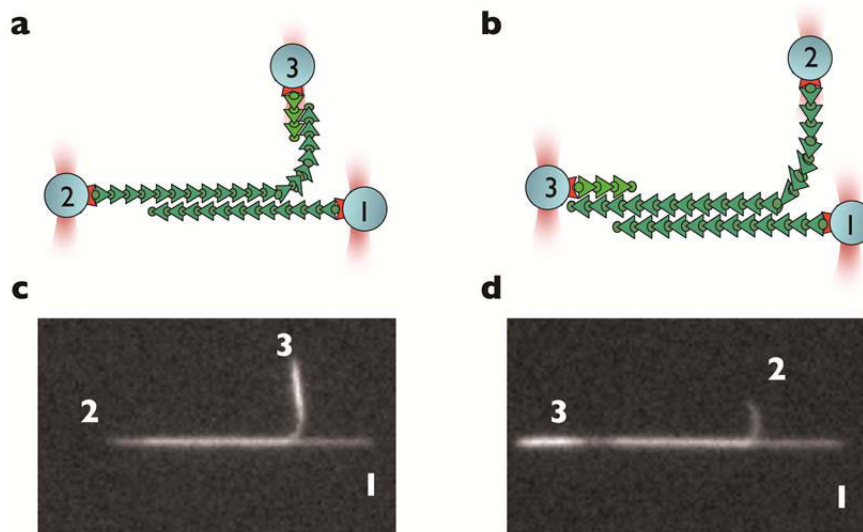


Figure 1. Adding non-adsorbing polymer to negatively charged actin filaments induces effective attractive interactions by the depletion mechanism. **A)** Adding non-adsorbing polymer exerts a uniform osmotic pressure on an isolated filament. A shell surrounding each filament excludes the center of mass of the depletion agent (PEG). As two filaments approach each other, the excluded volume shells overlap. Consequently there is an imbalance of osmotic pressure, which results in effective attractive interactions. The range and the strength of the depletion attraction can be controlled by changing the size and the concentration of the non-adsorbing polymers. **B)** Calculated pair potential between two aligned filaments at different PEG concentrations. **C)** In the presence of attractive interactions F-actin collapses into racquet-like structures. Images of actin racquets taken at three different PEG concentrations used for sliding experiments. Balancing adhesive interactions with filament elasticity estimates the binding energy per unit length. **D)** Adhesion energy as determined by analysis of racquet-like structures. The measured energies are significantly smaller than theoretical predictions in panel B due to the interpenetration of the filaments and depleting polymers as discussed in Ref. 11.



Supplementary Figure 2. Monomer hopping over a barrier is associated with the soliton formation which propagate along the filament. **A)** A kymograph illustrates temporal evolution of the tension (local filament compression) along the filament as it is pulled away from the periodic substrate. The pulling direction is to the right, while time evolution is downward. Each time a monomer is pulled over the rightmost barrier a soliton propagates along the filament enabling all the monomers to translate by one lattice unit. **B)** Zoomed in region demonstrates the propagation of a soliton, which carries local filament compression, along the filament contour. **C)** Another representation of filament configuration during propagation of a soliton. The x -axis represents the position along the filament contour while the y -axis is the local filament tension. For clarity filament conformations taken at different times are displaced along the y -axis. The dynamics of soliton propagation is illustrated in Movie S2.



Supplementary Figure 3. Schematic of the three bead experimental setup used to measure the directional dependence of sliding friction. **(A)** Illustration of an actin bundle in which filaments have antiparallel configuration. The relative filament orientation is controlled by attaching beads to both ends of one filament as discussed in the supporting methods section. **(B)** Configuration used to measure sliding friction of filaments with same polarity. The bright region indicates the pointed end of a long actin filament which is bundled with a multifilament short bundle. The polarity of the filament bundle is switched by reversing the positions of bead 2 and 3. **(C)** Experimental configuration used to determine friction of filaments with same polarity. The brighter region in the vicinity of bead 3 indicates the short multifilament bundle which is attached to the pointed end of the long isolated actin filament attached to bead 2. **(D)** The experimental configuration corresponding to schematic in panel B is used to measure the sliding friction of parallel filaments.

Supplementary Tables

PEG(%)	$A(\text{pN})$	$v_o(\text{nm/sec})$	$d(\text{nm})$
2.5	1.6 ± 0.3	6.4 ± 3	5.2 ± 1
3	1.4 ± 0.25	0.4 ± 0.3	5.8 ± 1
3.5	0.82 ± 0.6	$2.E-05 \pm 3.E-03$	10 ± 7.4
2-AP	1.5 ± 0.4	0.27 ± 0.4	5.4 ± 1.4
2-P	1.5 ± 0.3	3.9 ± 2	5.4 ± 1

Supplementary Table 1. Experimentally measured force-velocity curves shown in Fig. 1D and Fig. 3B are fitted to the Tomlinson model. This provides an estimate for the spacing of the background periodic potential. Error bars are the 95% confidence intervals for each fit parameter

Velocity	$\lambda_{exp}(\text{nm})$
40	1340
80	1300
180	1450

Supplementary Table 2. Comparison between the experimental kink width extracted from actin sliding runs done at three different pulling velocities

PEG(%)	$\lambda_{exp}(\text{nm})$	$\lambda_{theory}(\text{nm})$
3.5	820	2000 ± 400
3	1310	2800 ± 500
2.5	2170	3000 ± 600

Supplementary Table 3. Experimentally measured kink width extracted from actin pulling experiments is compared with theoretical estimates from our theoretical model. There are no adjustable parameters. Error bars for λ_{theory} are determined from standard error propagation of the parameters k , and U_o in the expression $\lambda^2 = kd^4/U_o$.

Supplementary Movies

Supplementary Movie S1

Assembly of an actin filament bundle, and the subsequent pulling experiment designed to measure polymer friction. Two gelsolin coated beads, each with an actin filament attached, are held in place with optical traps. Bead 1 attached to filament 1 is located on the left, while bead 2 attached to the filament 2 is located on the right. Flow is used to establish a contact between the pointed end of filament 1 and bead 2. The gelsolin coated bead transiently binds sideways to the filament 1. Immediately upon binding, the flow is reversed in the opposite direction causing filament 2 to rotate by 180° and bundle with filament 1 which is attached at both ends and thus is not affected by the external flow. Upon bundling, the region of increased brightness indicates the contact length between the two filaments. The gelsolin on bead 2 which is bound sideways to filament 1 eventually severs a portion of the filament off. At this point the filaments are free to slide. Bead 2 is moved at a constant velocity while simultaneously measuring force on the bead 1. The width of the image is $37\text{ }\mu\text{m}$.

Supplementary Movie S2

Computer simulations reveal the dynamics of a filament translocation. The height of the bead in the background sinusoidal potential represents the local filament tension. Initially, the applied tension to the rightmost bead decays exponentially along the filament contour. At sufficiently large force or equivalently after long enough time, as the rightmost bead crosses the final barrier, a soliton like structure is formed. It travels along the entire filament contour allowing for the entire filament to translocate by unit spacing.

Supplementary Movie S3

Fluctuations of a bundled actin filament pair confined to quasi-2D. Both filaments have been coated with polyethylene glycol (MW 2,000). Unlike bare F-actin, PEG coated filaments exhibit significant sliding due to thermal fluctuations. The region of increased brightness indicates the location of the shorter filament which is bound to the longer one. Tracking the center of the short filament determines the mean square displacement. From there it is possible to determine the diffusion coefficient of the short filament. The width of the image is $12.7\text{ }\mu\text{m}$ and the duration of the movie is 180 seconds.

References:

- 1 Maclean-Fletcher, S. & Pollard, T. D. Identification of a factor in conventional muscle actin preparation which inhibits actin filament self-association. *Biochemical and Biophysical Research Communications* **96**, 18-27, doi:10.1016/0006-291x(80)91175-4 (1980).
- 2 Pardee, J. D. & Spudich, J. A. Purification of muscle actin. *Methods in Cell Biology* **24**, 271-289 (1982).
- 3 Brangwynne, C. P. *et al.* Bending dynamics of fluctuating biopolymers probed by automated high-resolution filament tracking. *Biophysical Journal* **93**, 346-359, doi:10.1529/biophysj.106.096966 (2007).
- 4 De La Cruz, E. M. & Pollard, T. D. Kinetics and thermodynamics of phalloidin binding to actin filaments from three divergent species. *Biochemistry* **35**, 14054-14061, doi:10.1021/bi961047t (1996).
- 5 Kurokawa, H., Fujii, W., Ohmi, K., Sakurai, T. & Nonomura, Y. Simple and rapid purification of brevin. *Biochemical and Biophysical Research Communications* **168**, 451-457, doi:10.1016/0006-291x(90)92342-w (1990).
- 6 Suzuki, N., Miyata, H., Ishiwata, S. & Kinosita, K. Preparation of bead-tailed actin filaments: Estimation of the torque produced by the sliding force in an in vitro motility assay. *Biophysical Journal* **70**, 401-408 (1996).
- 7 Molloy, J. E. Optical chopsticks: Digital synthesis of multiple optical traps. *Methods in Cell Biology, Vol 55* **55**, 205-216 (1998).
- 8 Allersma, M. W., Gittes, F., deCastro, M. J., Stewart, R. J. & Schmidt, C. F. Two-dimensional tracking of ncd motility by back focal plane interferometry. *Biophysical Journal* **74**, 1074-1085 (1998).
- 9 Frenkel, D. & Smit, B. *Understanding Molecular Simulation From Algorithms to Applications*. (Academic Press, 1996).
- 10 Braun, O. M. & Kivshar, Y. S. Nonlinear dynamics of the Frenkel-Kontorova model. *Physics Reports-Review Section of Physics Letters* **306**, 1-108, doi:10.1016/s0370-1573(98)00029-5 (1998).